Analysis of Mode-Split Operation in MEMS Based on Piezoresistive Nanogauges

Giacomo Langfelder, Stefano Dellea, Audrey Berthelot, Patrice Rey, Alessandro Tocchio, and Antonio Francesco Longoni

I. Introduction

AMONG THE technological innovations in the field of MEMS sensors in the last decade, one possible approach is the combination of micrometric and nanometric elements in the same device. Such a process exploits relatively large suspended masses and springs (e.g. 20 μm-thick) to transfer forces to heavily-doped Silicon nano-gauges with a typical cross-section in the order of $(250\ \text{nm})^2$ and lengths in the order of a few μm [1]. Through suitable geometrical designs, a large stress concentration on the gauges can be obtained under external forces, which can be therefore detected through piezoresistive sensing. Device miniaturization can be obtained thanks to the small area of this sensing element, compared to arrays of capacitive sensing parallel plates. Descriptions of sensors based on piezoresistive nano-gauges and preliminary demonstration of their operation were given e.g. in [1]–[3].

Manuscript received January 8, 2014; revised April 27, 2014; accepted May 2, 2014. Date of publication June 12, 2014; date of current version January 30, 2015. This work was supported by the European Union through the FP7-ICT Programme Nine-Axis Inertial Sensor Based On Piezoresistive Nano-Gauge Detection Project under Grant 288318. Subject Editor S. Merlo.

G. Langfelder, S. Dellea, and A. F. Longoni are with the Department of Electronics, Information and Bioengineering, Politecnico di Milano, Milano 20133, Italy (e-mail: giacomo.langfelder@polimi.it; stefano.dellea@polimi.it; longoni@elet.polimi.it).

A. Berthelot and P. Rey are with Commissariat à l'Énergie Atomique et aux Énergies Alternatives-Leti Minatec, Grenoble 38054, France (e-mail: patrice.rey@cea.fr; audrey.berthelot@cea.fr).

A. Tocchio is with the Analog, MEMS, and Sensors Division, ST Microelectronics, Milano 20010, Italy (e-mail: alessandro.tocchio@st.com).

Color versions of one or more of the figures in this paper are available online.

The goal of this work is to deepen the characterization of this new process in terms of repeatability, through the analysis of a suitable structure (A). The device features a tuning-fork (TF) capacitive mode (where nano-gauges play no role in determining the resonance) and a piezoresistive sensing (PS) mode (whose frequency is by a large fraction determined by the nano-gauge constraint). With this device, it is possible to analyze the correlation between the TF and PS modes, i.e. the fluctuation in their difference from part to part, locally caused by process nonuniformities. A comparison is made with a reference structure (B), having a similar TF mode but a capacitive sensing (CS) mode, built in the ST Microelectronics surface micromachining process [4].

The interest of this analysis is in the fact that several devices in consumer applications operate with an intended mismatch between e.g. a drive and a sense mode, with a well-defined mode split [5]–[8]. In this condition, their sensitivity is proportional to the inverse of the modes difference, so that variations of the modes split from part to part correspondingly imply low repeatability in the value of the sensitivity over different samples.

Section II presents the two structures and their fabrication processes, and defines two sources of sensitivity fluctuations for devices based on Si nano-gauges (the gauge factor and the frequency split). In Section III, a gauge factor of about 50 is measured, with a $\pm 9\%$ maximum deviation evaluated across 10 samples. Section IV focuses on the results about modes correlation, obtained on 26 samples of type A and 14 samples of type B. It is shown how for structure B there is an almost unitary ($\pm 8\%$) correlation between the two modes, as the variance in the process height and etching locally affects in the same way the TF and CS modes. On the contrary, for structure A an imperfect correlation (variations up to $\pm 30\%$) in the PS mode with respect to the TF mode is observed, which demands new design guidelines. A theoretical analysis to explain the observed results on the basis of the technological corners, and new design guidelines for improved immunity to process nonuniformities are finally discussed in Section V.

II. Description of the Test Devices

Fig. 1 shows a schematic top-view of the structure. One can distinguish the tuning fork springs and, for each device half:

- an external frame with combs to actuate/sense the TF mode. Thanks to folded springs, the frame moves in the x-direction but it is highly constrained along the y-axis;

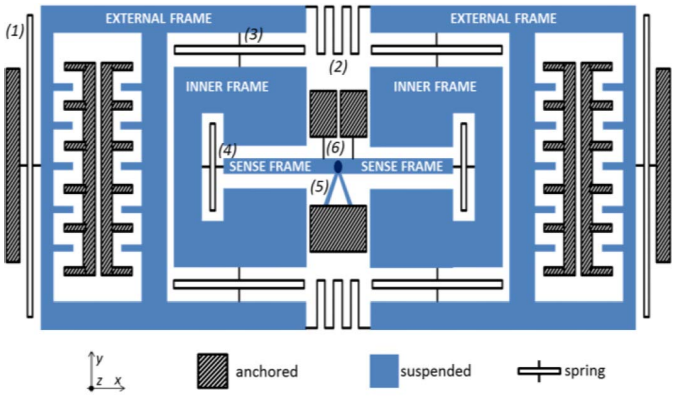

Fig. 1. Schematic view of a doubly decoupled tuning fork structure with a lever system and piezoresistive sensing elements (nano-gauges). Numbers indicate (1) drive springs, (2) tuning fork, (3) drive decoupling springs, (4) sense decoupling springs, (5) rotational hinge and (6) nano-gauges.

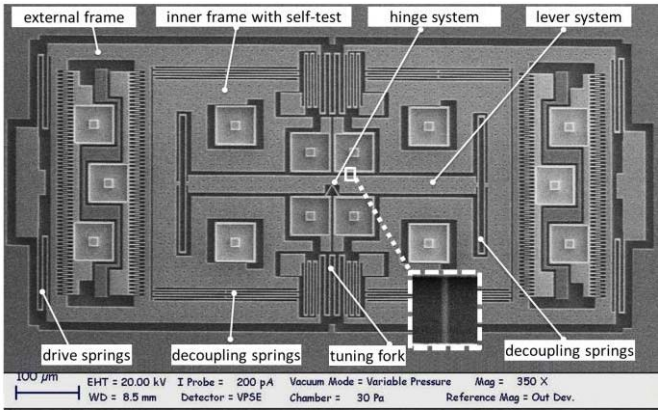

Fig. 2. SEM top-view image of the structure A tested in this work. A nano-gauge view is enlarged in the inset. With respect to the scheme of Fig. 1, four self-test electrodes are added inside the inner frames for electrostatic actuation.

- an inner decoupling frame, dragged in the horizontal direction during TF actuation, and free to move also in the y-direction thanks to the decoupling springs;
- a PS frame, decoupled from motion in the x-direction by suitable springs, and free to tilt around a hinge under differential displacements caused by the inner frame.

The PS lever is designed to transfer a differential stress to a pair of nano-gauges, designed close to the rotation point. The gauges position along the lever system is optimized in order to have the largest possible linear-range stress (a few hundred MPa) for a 50 nm target displacement of the lever tip. The need for a decoupled architecture comes from the fact that the gauges cannot stand large (e.g. a few μm) displacements in the x-direction.[1]

In general, the need for a lever scheme comes from the large axial stiffness of the nano-gauge: this would shift the PS mode to very high frequencies if directly coupled (with a y-axis orientation) to a translating PS frame.

The TF and PS modes are characterized by the resonance frequencies f_{TF} and f_S respectively. There are several examples of sensors (e.g. gyroscopes [7], [8] and recently magnetometers [9], [10]) operating in a mode-split condition, i.e. with a small difference Δf between f_{TF} and f_S. A piezoresistive sensor of a physical quantity Q, operated in a mode-split configuration, has a sensitivity proportional to the piezoresistive gauge factor GF and to the inverse of the modes split Δf [3], [6], [9]:

$$\frac{\Delta R}{\Delta Q} \propto \frac{GF}{\Delta f \cdot A_g} \tag{1}$$

In Eq. (1), the sensitivity is defined as the variation in the resistances ΔR per unit change ΔQ in the quantity to be measured (A_g is the gauge cross-section). The paper therefore considers GF and Δf as potential sources of variance in the sensitivity. Measurements of these parameters on different samples will be given in Section III and IV, after a description of the devices and fabrication processes used in this work.

[1]The device resembles a TF gyroscope [7], [8], [11]–[13]; however, operation under angular rates is not shown, as only wafer-level samples are available.

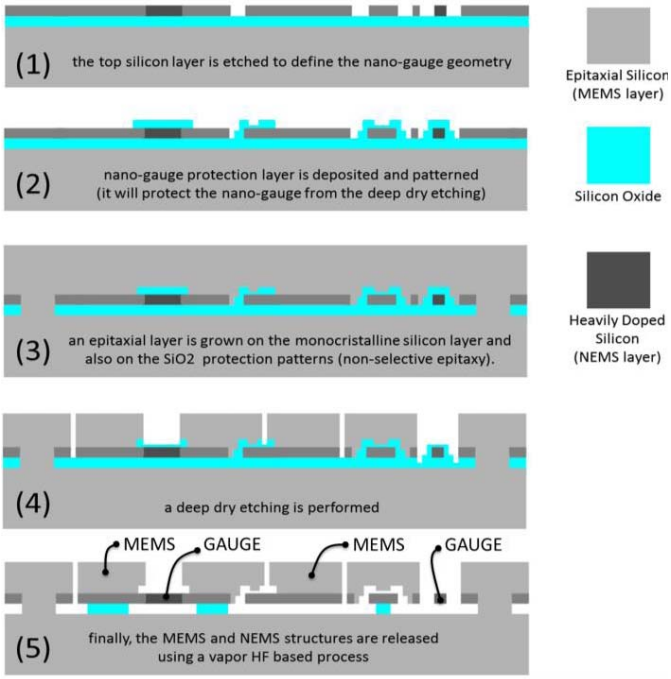

Fig. 3. Fabrication process flow for the realization of the structures with the piezoresistive sense mode based on nano-gauges. Details of the process steps highlighted in subplots (1)–(5) are given in the text.

A. Structure A (PS Sensing): Process and Description

The structure of major interest in this work, shown in the Scanning Electron Microscope (SEM) image of Fig. 2, features a pair of piezoresistive nano-gauges linked to a lever system, resembling the scheme presented in Fig. 1.

Its fabrication flow (Fig. 3) starts with a Silicon-on-insulator (SOI) substrate, with 1-μm-thick buried oxide and a 250-nm-thick mono-crystalline Silicon top layer. This heavily doped layer (resistivity 2.9 10^{-5} Ω·m) sets the nano-gauge thickness. In the first process step, a deep ultraviolet (DUV)

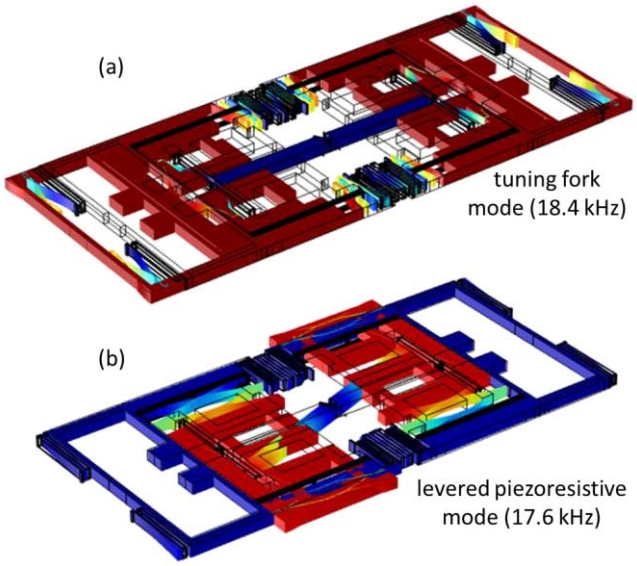

Fig. 4. Results of FEM eigenfrequency analyses of the type-A structure with a 20 μm height: (a) anti-phase TF mode; (b) levered sense mode.

lithography defines the nano-gauge layer planar geometry; the etching is obtained through reactive ion etching (RIE). Then, a 0.5-μm-thick oxide is deposited where the gauge layer must be separated from the micrometric structures, defined in the next process steps. Lithography and RIE etching of this oxide only maintain this layer on top of nano-gauges.

Thick non-selective epitaxial growth is then done, both on the crystalline Silicon and on the SiO_2 layer lying on top of the gauges, to form the 20-μm-thick MEMS part. A lithography step and a deep RIE (DRIE) of the epitaxial layer are operated as in standard processes to define the MEMS structures and to open the SiO_2 protective layer of the nano-gauges. Finally, the sensor release is achieved by hydrofluoric acid (HF) vapor etching. More details on the process can be found in [1] and [14].

For the given process height, the nominal minimum width for the micrometric suspended parts is 1 μm, with minimum gaps of 750 nm.

The overall dimensions of structure A are 915 μm $\times$ 443 μm. The nano-gauge cross section is $(250\ \text{nm})^2$. Within the inner frame, further electrodes are designed as electrostatic self-test of the PS mode.

Finite element method (FEM) 3-D simulations were performed for the modal analysis of the device. At least five elements were used across the smallest features (springs and nano-gauges). An equivalent density was used for the material of the suspended mass to account for the $(2\ \mu\text{m})^2$ holes needed for the release. Comb fingers were condensed in a single block to save computational complexity. Fig. 4 reports the anti-phase TF mode and the levered PS mode, which are of interest for this work. In particular, the design frequency for the TF mode falls at 18.4 kHz, with the PS mode frequency at 17.6 kHz, resulting in a nominal mismatch $\Delta f = 0.8$ kHz.

B. Structure B – (Standard Micromachining Process)

The second structure is built with the ST Microelectronics ThELMA (Thick Epitaxial Layer for Microactuators and Accelerometers) surface micromachining, well described e.g. in [4]. The process has a minimum feature for suspended widths and gaps of ~ 2 μm. It allows the realization of suspended structures with a polysilicon structural layer thickness (22 μm) comparable to the process described above.

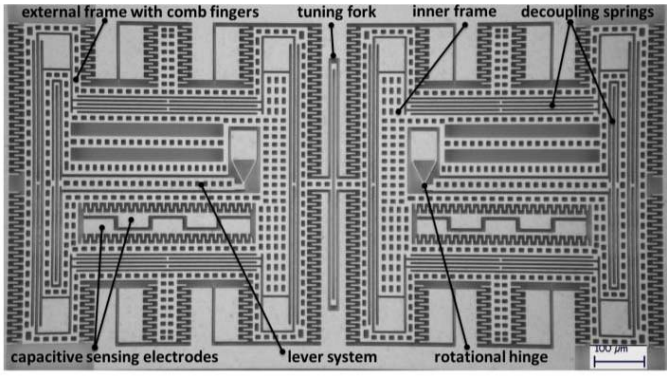

Fig. 5. Optical microscope top-view image of structure B tested in this work.

The fabrication begins with a thermal treatment at 1100 °C of the substrate, to create a 2-μm-thick thermal, sacrificial, oxide layer. Deposition and patterning of 750-nm-thick horizontal interconnections are performed to define the buried runners, which are used to bring electrical signals outside the device. Deposition, patterning and planarization of a further 2.6-μm-thick SiO_2 sacrificial layer is obtained through Plasma Enhanced Chemical Vapor Deposition. The epitaxial polysilicon structural layer is grown in the reactors, reaching a 22-μm thickness. This structural layer is patterned by DRIE trench anisotropic etching, to reach the oxide layer. Finally, dry HF sacrificial oxide removal and contact metallization deposition concludes the processing of the MEMS wafer (see [15] for more details). Wafer-wafer packaging and dicing steps are not performed for the devices of this work.

Structure B too (Fig. 5) resembles the scheme of Fig. 1, having an anti-phase comb-driven TF mode and a levered (even if decoupled) sense mode (see the optical image of Fig. 2(b)). The major difference from structure A is in that here the readout is obtained through capacitive pick-off electrodes, so that both the TF and the CS modes depends on springs of the same structural layer and with similar widths (1.9 μm).

The overall device dimensions are 885 μm $\times$ 370 μm, with the mentioned height of 22 μm. The minimum hole area is $(4\ \mu\text{m})^2$. FEM simulations predict a nominal frequency mismatch $\Delta f \sim 2$ kHz (25.1 kHz for the anti-phase drive mode and 27.1 kHz for the sense mode).

It is worth noting that several fabrication steps of structure A, which allows nano-gauge readout, are common to those of the standard micromachining process given in this Section. Fig. 6 reports two SEM images at the same enlargement, showing in both cases a suspended mass facing a fixed part, and the presence of sub-micrometric thin layers. In both processes, sidewall scallops and footing effects are negligible, with a resulting sharp profile of the epitaxial Silicon after the DRIE. Therefore, such process imperfections will not be considered as relevant in the following analysis.

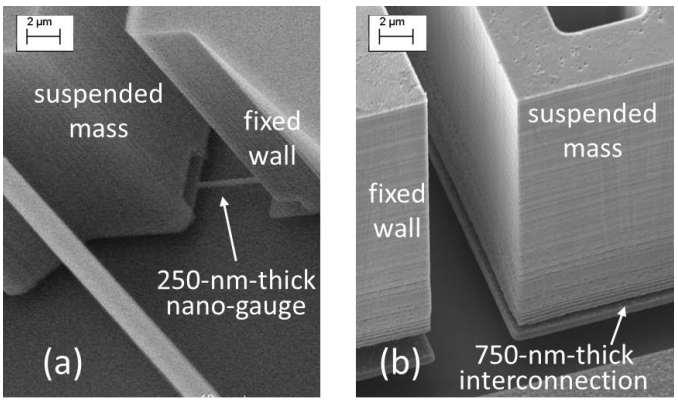

Fig. 6. SEM pictures showing similar sharp vertical profiles (with almost non-visible scallops and footing) obtained in the process with nano-gauges (a) and in the ST Microelectronics process (b).

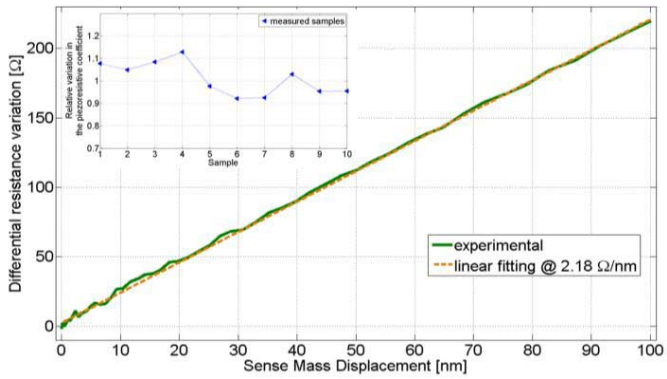

Fig. 7. Differential resistance variation as a function of the inner frame displacement. The inset shows the measurement repeatability over 10 samples.

III. Gauge-Factor Repeatability

The gauge-factor is a parameter that determines the sensitivity of a sensor based on piezoresistive nano-gauges, as shown in Eq. (1) (see also [1], [3], [14]). As it is a qualifying parameter for the process discussed in this work, its repeatability is first analyzed.

Measurements of the gauge factor were thus performed on Structure A using the self-test actuators. There are four self-test electrodes, two per half structure, separated by 1 μm gap from the frames. By actuating two opposite self-test electrodes through quasi-stationary increasing voltage, the inner frames displace in opposite directions, making the lever rotate around the hinge. The other electrodes can be used for capacitive detection, so that a calibration of the effective displacement of the inner frames under the electrostatic actuation voltage can be done in parallel to the piezoresistive readout. This is a key point for the correct estimation of the gauge factor.

Fig. 7 reports a sample measured differential resistance variation with respect to the displacement in the sense direction, indicating *(i)* a scale-factor for the PS mode of about 2.2 **Ω**/nm, and *(ii)* a linearity error (calculated as the relative deviation from the best linear fitting) lower than 1.5%. Through the lever transduction factor (0.072), the nano-gauge length (5 μm) and the resistance value at rest (2.8 k**Ω**) one can evaluate a corresponding gauge-factor $GF = 50.2$. The repeatability of the measurement is within $\pm 9\%$ over 10 tested samples (see the inset in the figure). As the same degree of variability is obtained by measuring the displacement through the two remaining capacitive electrodes, these measurements lead to the conclusion that the differential gauge factor is quite stable over different samples.

IV. Drive and Sense Modes Correlation

The repeatability analysis continues with the measurements of the mismatch Δf for the two described structures. Though this parameter is common to capacitive sensors, its constancy across devices based on piezoresistive sensing is markedly different, as shown and motivated in this Section.

Indeed, in devices like structure A, in order to maximize the stress on the gauges during the motion of the inner frame, their position along the lever gives rise to a non-negligible constraint with respect to the overall constraint of the sense mode. This means that the resonance frequency f_S of the PS mode depends not only on the micrometric springs and hinge, but also on the nano-gauges themselves. On the other side, the TF mode frequency f_{TF} depends only on micrometric springs. Nonuniformities in the epitaxy height or etching may induce an imperfect correlation between the two modes, thus variations of the mismatch Δf from part to part, which cannot be ignored when high repeatability in the sensitivity is desired.

The measurements presented in this Section were obtained on bare wafers, at a probe station with manual probe positioners. All the data were collected in a clean room, monitored environment, at a temperature of 25$\pm$2°C. Measurements of the natural frequency of the modes were done using the setup described in [16] and [17]. The technique is based on the excitation of a mode through electrostatic actuation, consisting in a slowly increasing voltage followed by a sudden voltage zeroing, to measure the natural oscillation after this downward electrostatic force step.

The electromechanical parameters can be then extracted by first applying a Fast Fourier Transformation (FFT) to the measured time response, and by subsequently fitting the data with the theoretical curve, with iterations on the values of the quality factor and resonance frequency, around the initial guess found by the FFT. The second part of the procedure greatly increases the precision in the parameters estimation.

For the TF mode measurement, the actuation signal is applied to a set of comb drives, and the readout electronics is connected to a second set of combs, for capacitive readout. The amplitude of the applied excitation voltage is ~30 V, corresponding to roughly $x = 1$ μm of displacement for the external and inner frames in the x-direction.

For the PS mode measurement, the actuation signal is applied to a pair of self-test electrodes and the readout electronics is connected to the nano-gauges, for piezoresistive readout. The applied voltage value is ~14 V, corresponding to roughly $\Delta y \sim 50$ nm of displacement (overshoot included) for each inner frame and lever tip, in opposite y-directions.

A. Structure A (M&NEMS Process)

Sample results of these measurements are reported in Fig. 8 and 9 for the drive and sense modes respectively. For each figure, the (a) label plots the measured curve, and the (b) label

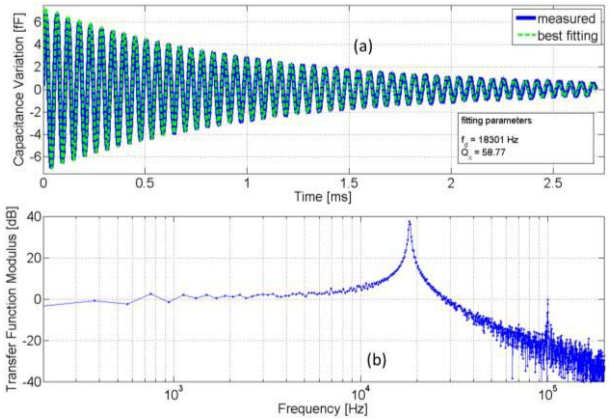

Fig. 8. Experimental results showing (a) the response to a downward step to the rest position, together with the best fitting curve, for the drive mode and (b) the corresponding FFT.

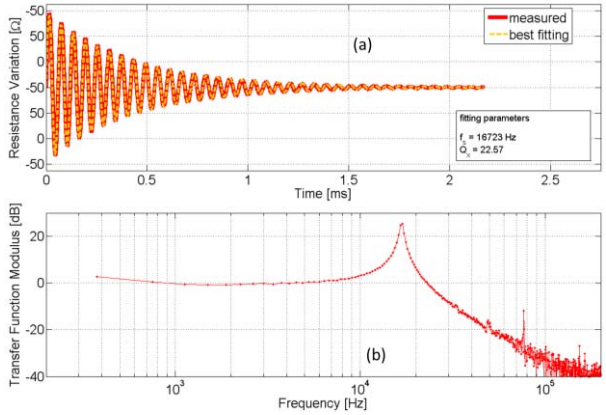

Fig. 9. Experimental results showing (a) the time response to a downward step to the rest position, together with the best fitting curve, for the sense mode and (b) the corresponding FFT.

plots the derived FFT. Starting from the parameters found by the FFT, (a) also reports the best-fitting damped waveform, indicating the found resonance and quality factor.

The measurements were repeated for 26 samples distributed on two wafers as indicated in the inset of Fig. 10(a). The on-wafer sample distance is 21 mm; non-numbered boxes marked in red represent non-working devices, likely due to incomplete release of a corner of the external frame, as inferred from IR microscope inspection. Overall, for the samples analyzed on two wafers the yield is in the order of 75%. The found average frequency for the TF mode is $f_{TF} = 18.3$ kHz, in line with the FEM simulation. The sense frequency is on average $f_S = 16.9$ kHz, slightly lower than predictions. Fig. 10(a) summarizes the obtained results, showing in square markers the measured TF mode and in circle markers the PS mode.

It is evident that there is a correlation between the frequency variations across the samples, but it is not unitary. Though the trend is similar, the drive mode shows a larger relative variation than the sense mode. This is made clearer in Fig. 10(b) (upside-down triangles), which reports, for each tested sample i, the relative deviation of the mismatch from its average value, $(\Delta f_i - \overline{\Delta f})/\overline{\Delta f}$. Deviations up to about $\pm 30\%$ can be observed with a minimum value of $\Delta f_{min} = 1.08$ kHz and a maximum value of $\Delta f_{max} = 1.87$ kHz. For the first

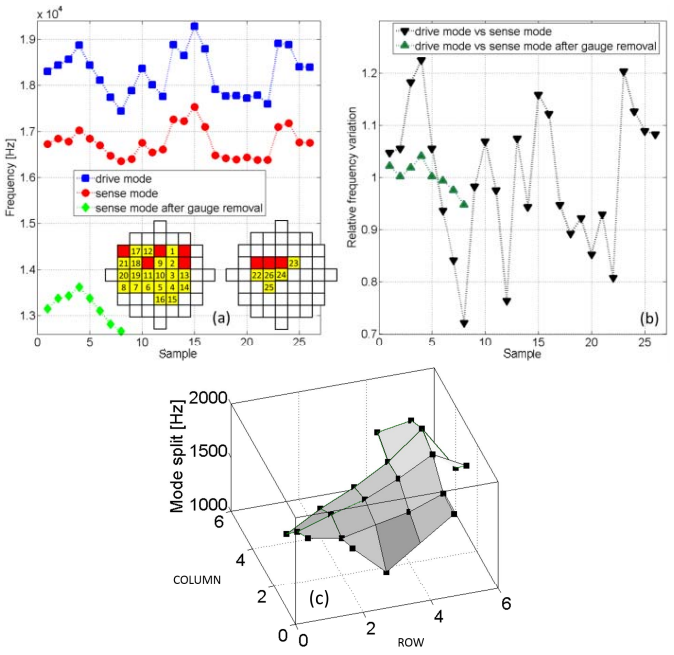

Fig. 10. (a) Measured resonance frequencies of 26 samples for the TF mode (squares), the PS mode (circles) and the sense mode after nano-gauge removal (diamonds, 8 samples); (b) relative deviation of the mismatch from the average value, with and without nano-gauges; (c) distribution of the Δf on wafer #1.

wafer, to which the largest number of tested samples belongs, the absolute frequencies as well as the Δf increase following a wafer border-to-center direction (Fig. 10(c)), which may indicate either an increased over-etching or a decreased epitaxy height towards wafer borders (see the next Section).

Looking back at Eq. (1) and considering the results obtained on the gauge factor variance, the measured mismatch fluctuation from sample to sample appears as the major source of sensitivity fluctuation among different samples. One possible reason to explain the observed behavior is the presence of nano-gauge constraints on the sense mode only, due to the fact that the $(250\ \text{nm})^2$ gauges are etched in a different step with respect to the epitaxial layer DRIE.

In order to confirm this hypothesis, the following operations were performed on 8 of the tested samples. The nano-gauges were connected to an electrometer (Keithley 617) one at a time. First, their resistance under a small current was measured. Then, the current was increased up to such values that the nano-gauges were burned (visual inspection confirmed the burnout). A high-impedance was found when measuring again the resistance.

The devices at this point were constrained only by springs of the micrometric type also for the sense mode. As in the previous case, downward step response measurements for the sense mode were obtained, this time using the self-test electrodes both for driving and for capacitive sensing. A sample obtained result is reported in Fig. 11. The data for these 8 devices are collected in Fig. 10(a) in diamond markers, showing an average frequency of 13.1 kHz now that the nano-gauge constraints are lost.

Fig. 10(b) also reports (green triangles) the relative deviation of the mismatch from its average value, for the samples

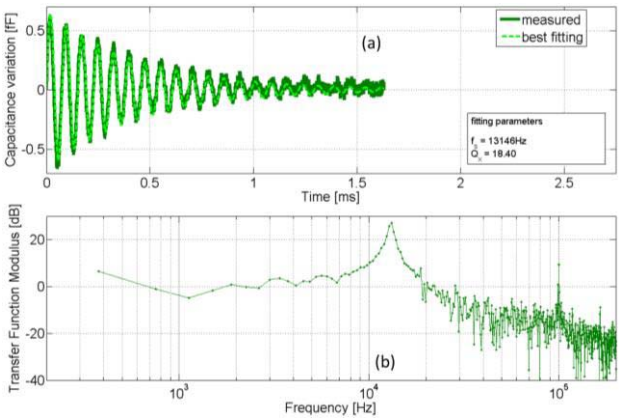

Fig. 11. Experimental results showing (a) the time response to a downward step to the rest position, together with the best fitting curve, for the sense mode after the nano-gauge elimination and (b) the corresponding FFT.

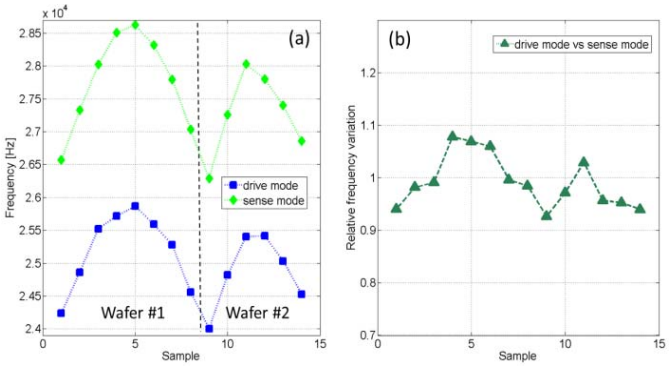

Fig. 12. (a) Measured resonance frequencies on 14 samples for the TF mode (squares) and the CS mode for the structure built in the ThELMA process; (b) relative deviation of the mismatch Δf from its average value.

modified after the removal of nano-gauges. The correlation between the frequencies turns now to be almost unitary, with a relative deviation in the order of $\pm 5\%$, which confirms the anticipated hypothesis.

B. Structure B (Standard Micromachining Process)

For further comparative purposes, the same kind of measurement was repeated on the structures of type B, which adopt capacitive pick-off electrodes for the sense mode. In general, for capacitive sensors (e.g. gyroscopes [7], [8], [11]–[13]), typical repeatability guidelines are to design the springs determining the TF and CS modes with the same (or very similar) width. In this way, local process imperfections have a well-correlated impact on the modes stiffness. In other words, different samples may have different absolute values of the same mode, but the mismatch Δf is expected to be quite stable across a wafer and from wafer to wafer.

In agreement with these predictions, 14 samples of structure B, belonging to two wafers, were tested (Fig. 12(a)). The results show an average split Δf of 2.5 kHz, slightly larger than predicted but much more stable from part to part, as indicated by mismatch relative deviations lower than $\pm 8\%$ of Fig. 12(b). In this case too, lower frequencies are found at wafer borders.

V. Predictions for Different Springs Geometries

In order to quantitatively assess the observed behavior and to be able to predict the fluctuation of the mismatch Δf as a function of the process corners and of the design geometry, several measurements of the epitaxy height and of the micrometric layer etching uniformity were gathered and correlated to the data of the previous section.

The average epitaxy height after planarization on the examined wafers is 20.2 μm, with a $\pm 3\sigma$ confidence interval of ± 1.3 μm. The etching uniformity of the micrometric layer was statistically assessed on 4 previously fabricated lots, through suitably developed *delta-width* networks. The measurements show an average over-etching value of about 30 nm, with a $\pm 3\sigma$ confidence interval of ± 81 nm. Similarly, delta-width networks were designed also for the nano-gauge layer. Measurements on the nano-gauge width revealed a ± 15 nm fabrication precision.

A model was developed to theoretically predict the stiffness (and the mass) of the two modes of structure A as a function of the epitaxy height and etching. In particular, for the TF mode with flexural folded springs with a width w_{TF} and an overall stiffness k_{TF}, the relative variation dk_{TF}/k_{TF} depends on the relative height variation *dh/h* and on the relative etching variation *de/e* according to:

$$\frac{dk_{TF}}{k_{TF}} = \frac{dh}{h} \tag{2}$$

$$\frac{dk_{TF}}{k_{TF}} = -3\frac{de}{w_{TF} - e} \tag{3}$$

A similar procedure was used for the PS mode. In this case, the contribution $k_{ng-lever}$ of the nano-gauge-constrained lever to the stiffness k_{PS} was estimated through FEM simulations, whose parametric results were incorporated in the model. The PS mode variation as a function of the height and etching non-uniformities is now:

$$\frac{dk_{PS}}{k_{PS}} = \frac{dh}{h}\left(1 - \frac{k_{ng-lever}}{k_{PS}}\right) \tag{4}$$

$$\frac{dk_{PS}}{k_{PS}} = -3\frac{de}{(w_{PS} - e)}\left(1 - \frac{k_{ng-lever}}{k_{PS}}\right) \tag{5}$$

Assuming a quite stable nano-gauge stiffness (as inferred from the measurements of Section III), the formulas (2)–(5) above quantify the different dependence of the TF and PS modes stiffness from the considered process nonuniformities.

The model output is represented by the frequencies of the two modes. Figure 13a reports them as a function of the etching, within its maximum and minimum corners reported above, plotting the TF mode as a dashed curve, the PS mode as a dot curve, and the sense mode with no gauges as an asterisk-marker curve. The absolute frequency values for no over or under etching are in reasonable agreement with FEM simulations and experimental data. Moreover, the results on the variation of the mismatch are well in line with the experimental measurements of the previous section, indeed:

(i) the correlation between the drive and sense modes is not unitary, and a maximum difference $\Delta f_{max} - \Delta f_{min} =$ 700 Hz is found for the maximum and minimum etching

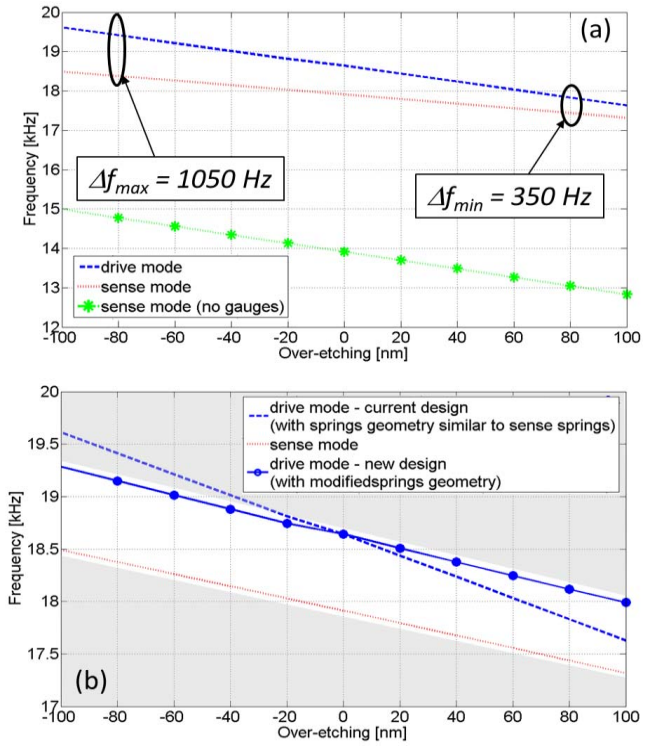

Fig. 13. (a) Model results for TF and PS modes (with and without gauges) as a function of the structural layer over-etch, using the same width for the micrometric springs of both the modes. The model predicts a maximum variability in the Δf of 700 Hz; (b) model results for TF and PS modes, using new design guidelines for the TF mode springs, to mitigate the Δf variability.

corners ($\pm$80 nm). This value well compares to the experimentally observed difference of $\Delta f_{max} - \Delta f_{min} =$ 790 Hz (Fig. 10(a));

(ii) as expected, the correlation between the drive and the sense modes when the effect of gauges is not considered turns back to be almost unitary.

The same procedure was repeated to take into account the effects of the process height corners, which result to have a lower impact (variation in Δf is lower than $\pm$200 Hz) as the stiffness of the springs of in-plane devices depends linearly on height and cubically on width, as shown by Eq. (2) and (3).

Two approaches are under consideration in order to relieve the observed effect, which degrades the repeatability in the gain-factor among different samples. The first one is suggested by formulas (2)–(5), and consists in using wider (and correspondingly longer) springs for the TF mode with respect to the PS mode ($w_{TF} > w_{PS}$). It is a different design guideline with respect to capacitive sensors, where TF and CS modes ideally claim for the same spring width, so to be affected in the same way by process variations. This new guideline is quite effective in solving the dependence of the Δf on the etching, but it leaves unsolved the (small) residual dependence on the variations in the process height. According to the model results and by equating Eq. (3) and (5), an increase by a factor 1.65 of the drive springs width and length is enough to make negligible the dependence of the Δf on the etching, as shown in Fig. 13b through circle markers. For the specific geometry shown in Fig. 1, such a spring length increase implies a partial increase of the overall device area (from 915 μm $\times$ 443 μm to 930 μm $\times$ 600 μm), mostly due to the space needed to lengthen the tuning fork folds.

The second approach, which is currently under analysis, is the introduction of nano-gauge elements also for the TF mode. This approach has a low impact on the device miniaturization and could allow the use of nano-gauges as TF mode detection elements (e.g. to close the drive loop in gyroscopes [18], [19]). This architecture requires a lever system also for the TF mode, and a similar weight-ratio of the nano-gauge stiffness to the overall stiffness for both the modes ($k_{ng-TF}/k_{TF} = k_{ng-lever}/k_{PS}$), in order to get well-correlated variations for different samples. Such a solution is also immune from process height changes.

It is however not straightforward to design nano-gauges in the TF mode: considering again the example of a gyroscope, while the inner mass displacement at full-scale could be in the order of a few tens of nm in the y-direction, the TF mass displacement (in the x-direction) is typically about 100 times larger [11]–[13].

This consideration implies that, if the nano-gauges are supposed to have the same weight in determining the stiffness (which is mandatory to solve the Δf fluctuations issue), than the gauges included in the drive mode will take 100 times the stress of the gauges put in the sense mode. This means roughly 10 GPa, which is both beyond the nominal tensile strength of the materials used for the gauges (typically $<$ 8 GPa for monocristalline Silicon), and 6 times larger than the buckling stress in compression ($\sim$ 2 GPa for the used gauge geometry), and 7 times larger than the maximum acceptable stress to avoid fatigue failure within 5 years of operation (1.4 GPa) [20]. Though different geometries may be studied, the implementation of such a solution appears as very challenging.

VI. Conclusion

This work investigated the repeatability of the gauge-factor and of the mode-split in a suitable device built in a process that employs piezoresistive nano-gauges as detection means.

Results demonstrated a repeatability of the mode-split more than three times poorer than in a standard micromachining process, based on capacitive sensing. The reason was found in that over-etching (mostly) and height (with a lower impact) differently affect modes with and without nano-gauges.

The observed fluctuation in the frequencies difference from part to part is predicted to be the main source of sensitivity fluctuations from part to part for sensors based on piezoresistive nano-gauges and operating in mode-split configurations.

Techniques to reduce the relevance of this issue were investigated and new design guidelines were derived for the springs, which differ from typical design guidelines of capacitive sensors.

Further studies on alternative geometries and on the impact of the fabrication nonuniformities on specific structures (accelerometers, gyroscopes and magnetometers) represent future work.

ACKNOWLEDGMENT

The authors gratefully thank Dr. N. Aresi and F. Souchon for helping with the setup preparation and the measurements.

REFERENCES

[1] P. Robert *et al.*, "M&NEMS: A new approach for ultra-low cost 3D inertial sensor," in *Proc. IEEE Sensors Conf.*, Christchurch, New Zealand, Oct. 2009, pp. 963–966.

[2] A. Walther, C. Le Blanc, N. Delorme, Y. Deimerly, R. Anciant, and J. Willemin, "Bias contributions in a MEMS tuning fork gyroscope," *J. Microelectromech. Syst.*, vol. 22, no. 2, pp. 303–308, Apr. 2013.

[3] A. Walther *et al.*, "3-axis gyroscope with Si nanogage piezo-resistive detection," in *Proc. IEEE MEMS Conf.*, Paris, France, Jan./Feb. 2012, pp. 480–483.

[4] G. Langfelder, S. Dellea, F. Zaraga, D. Cucchi, and M. A. Urquia, "The dependence of fatigue in microelectromechanical systems on the environment and the industrial packaging," *IEEE Trans. Ind. Electron.*, vol. 59, no. 12, pp. 4938–4948, Dec. 2012.

[5] V. Kempe, "Gyroscopes," in *Inertial MEMS Principles and Practice*. Cambridge, U.K.: Cambridge Univ. Press, 2011, Ch. 8.

[6] C. Acar, A. R. Schofield, A. A. Trusov, L. E. Costlow, and A. M. Shkel, "Environmentally robust MEMS vibratory gyroscopes for automotive applications," *IEEE Sensors J.*, vol. 9, no. 12, pp. 1895–1906, Dec. 2009.

[7] G. Langfelder and A. Tocchio, "Operation of Lorentz-force MEMS magnetometers with a frequency offset between driving current and mechanical resonance," *IEEE Trans. Magn.*, vol. 50, no. 1, p. 4700106, Jan. 2014.

[8] G. Langfelder, P. Minotti, G. Laghi, A. Tocchio, and A. Longoni, "Off-resonance, low-pressure operation of Lorentz force MEMS magnetometers," *IEEE Trans. Ind. Electron.*, to be published, doi: 10.1109/TIE.2014.2317153.

[9] S. E. Alper and T. Akin, "A single-crystal silicon symmetrical and decoupled MEMS gyroscope on an insulating substrate," *J. Microelectromech. Syst.*, vol. 14, no. 4, pp. 707–717, Aug. 2005.

[10] N. Yazdi, F. Ayazi, and K. Naja, "Micromachined inertial sensors," *Proc. IEEE*, vol. 86, no. 8, p. 16401659, Aug. 1998.

[11] A. A. Trusov, A. R. Schofield, and A. M. Shkel, "Gyroscope architecture with structurally forced anti-phase drive-mode and linearly coupled anti-phase sense-mode," in *Proc. IEEE Transducers Solid-State Sens., Actuators, Microsyst. Conf.*, Denver, CO, USA, Jun. 2009, pp. 660–663.

[12] R. Neul *et al.*, "Micromachined angular rate sensors for automotive applications," *IEEE Sensors J.*, vol. 7, no. 2, pp. 302–309, Feb. 2007.

[13] Z. Y. Guo, L. T. Lin, Q. C. Zhao, Z. C. Yang, H. Xie, and G. Z. Yan, "A lateral–axis microelectromechanical tuning–fork gyroscope with decoupled comb drive operating at atmospheric pressure," *J. Microelectromech. Syst.*, vol. 19, no. 3, pp. 458–468, Jun. 2010.

[14] D. Ettelt, P. Rey, G. Jourdan, A. Walther, P. Robert, and J. Delamare, "3D magnetic field sensor concept for use in inertial measurement units (IMUs)," *J. Microelectromech. Syst.*, vol. 23, no. 2, pp. 324–333, Apr. 2014.

[15] G. Langfelder, A. Longoni, A. Tocchio, and E. Lasalandra, "MEMS motion sensors based on the variations of the fringe capacitances," *IEEE Sensors J.*, vol. 11, no. 4, pp. 1069–1077, Apr. 2011.

[16] C. Buffa, A. Tocchio, and G. Langfelder, "A versatile instrument for the characterization of capacitive micro- and nanoelectromechanical systems," *IEEE Trans. Instrum. Meas.*, vol. 61, no. 7, pp. 2012–2021, Jul. 2012.

[17] ITMEMS s.r.l., Milano, Italy. (2014, May). *MEMS Characterization Platform, MCP-A-04, Product Data-Sheet* [Online]. Available: http://www.itmems.it

[18] C. D. Ezekwe and B. E. Boser, "A mode-matching closed-loop vibratory-gyroscope readout interface with a 0.004°/s/$\sqrt{\text{Hz}}$ noise floor over a 50 Hz band," in *Proc. ISSCC*, 2008, pp. 580–581.

[19] A. Sharma, M. F. Zaman, and F. Ayazi, "A sub-0.2 °/hr bias drift micromechanical silicon gyroscope with automatic CMOS mode-matching," *IEEE J. Solid-State Circuits*, vol. 44, no. 5, pp. 1593–1608, May 2009.

[20] G. Langfelder, S. Dellea, P. Rey, A. Berthelot, and A. Longoni, "Investigation of the fatigue origin and propagation in submicrometric silicon piezoresistive layers," in *Proc. IEEE MEMS Conf.*, San Francisco, CA, USA, Jan. 2014, pp. 640–643.